Princeton/$\mu\mu$/**99-19**

A Low-Pressure Time-Projection Chamber

Hulya Guler

A SENIOR THESIS
PRESENTED TO THE FACULTY
OF PRINCETON UNIVERSITY
IN CANDIDACY FOR THE DEGREE
OF BACHELOR OF ARTS

RECOMMENDED FOR ACCEPTANCE
BY THE DEPARTMENT OF
PHYSICS

THIS THESIS REPRESENTS MY OWN WORK
IN ACCORDANCE WITH UNIVERSITY REGULATIONS.

APRIL 1999

Abstract

A low-pressure time-projection chamber (TPC) prototype has been designed and built in order to determine the feasibility of employing low-pressure TPC's in the Muon Collider Collaboration's ionization cooling experiment. The chamber's longitudinal resolution at zero magnetic field has been measured at pressures below 50 torr with methane, ethane, and isobutane. Longitudinal diffusion in the chamber has been observed to decrease approximately steadily as the ratio of electric field to pressure is increased. This observation does not agree with data which has previously been recorded with methane at atmospheric pressure.

Acknowledgments

The low-pressure TPC project is a collaborative effort and as such has provided me with the opportunity to work closely with several admirable physicists. I am indebted to the following people for making this thesis a substantial and exciting learning experience:

Professor Kirk McDonald has given me valuable guidance throughout the project, always pointing out ways in which I could improve my work, and kindly reading and commenting on my reports, sometimes even at early hours of the morning. Most importantly he has taught me what it means to make a good measurement.

It was both inspiring and instructive to work with Professor Eric Prebys, who in a few minutes can produce code that can take me days and days to understand. My hope is that some day I will also be able to work at such high speeds. I am grateful for his encouragement, which made me feel good about my work whenever I began pointlessly fretting about how much more work I should have done.

It was a pleasure to work with Dr. Changguo Lu on building a working detector. It is educational just to see the way he sets up an experiment. From him I learned that it is a great skill to avoid making a mistake that might ruin all previous work, and that diligence is an important part of being an experimental physicist.

I would also like to express my appreciation for the help Dr. Stan Chidzik has provided throughout the course of my thesis work, especially on my schematic and layout of the converter board for the readout of the TPC.

I am also grateful to Professor Daniel Marlow, who was the one to recommend that I work on this project; he was always there (perhaps in Japan, perhaps in Norway, but always reachable by e-mail) to answer my random questions, and provided encouragement and valuable advice.

Finally, I must thank two people who indirectly influenced my work on this thesis. My mother Sema Gür, who sacrificed years of her life for my benefit and provided moral support throughout my four years at Princeton. And my grandmother Hatice Gür, whose values and principles have shaped my personality. Were it not for these two people, I would not be writing these words.

Dünyada her şey için, medeniyet için, hayat için, muvaffakiyet için en hakiki mürşit ilimdir, fendir. İlim ve fennin haricinde mürşit aramak gaflettir, cehalettir, dalalettir.

Mustafa Kemal Atatürk

Contents

Chapter 1

Introduction

Recently, the need for a detector with a minimal accidental-scattering rate to measure muon trajectories in the Muon Collider Collaboration's ionization-cooling experiment has motivated a group at Princeton University[1] to examine the possibility of operating a time-projection chamber (TPC) at low pressures [L+97]. The TPC, the typical geometry of which is sketched in Fig. 2.1, is a type of particle detector in which uniform and parallel electric and magnetic fields are applied to a drift volume that contains no detection units. When a charged particle passes through the drift volume, it ionizes molecules along its path, and the electrons thus released drift into a detection region where they produce avalanches on high-voltage anode wires. The distribution of the image charge collected on a plane of cathode pads parallel to the anode wires, combined with the time of arrival of the electrons, yields the three-dimensional trajectory of the initial charged particle.

The time-projection chamber has traditionally been operated with gas at atmospheric or high pressures. No record exists of a previous experimental test of the effect of low pressures on the resolution with which a TPC can reconstruct particle trajectories. This thesis presents measurements of the longitudinal position resolution of a prototype TPC

[1] C.Lu, K.T. McDonald, E.J. Prebys, S.E. Vahsen and the author.

that has been tested at pressures below 50 torr[2].

This chapter will review the motivation for building a muon collider and provide a brief outline of the Muon Collider Collaboration's proposed ionization-cooling experiment.

1.1 The Muon Collider: Motivation

High-energy particle accelerators that have been built to date have collided proton beams ($\bar{p}p$ or pp), electron beams (e^+e^-), and both (ep). Although proton colliders have succeeded in reaching higher energies than e^+e^- colliders, the reactions ensuing from proton collisions involve the protons' constituent quarks and often take place at energies much smaller than the available machine energy; moreover, they are complicated and need to be distinguished from large backgrounds. In contrast, electron machines generate lower backgrounds and produce simpler interactions involving only the point-like electrons and positrons at the full machine energy [PG97].

The possibility of colliding muon beams was first suggested by Skrinsky et al. [PS83, SP81] and by Neuffer [Neu83]. Since muons are essentially heavy electrons, a muon collider would have the same advantages over proton machines as an e^+e^- collider. While the physics that can be explored with a $\mu^+\mu^-$ collider is similar to the physics explored by e^+e^- colliders, the $\mu^+\mu^-$ collider is superior in several respects.

The foremost advantage of colliding muons instead of electrons is that in a circular accelerator, a muon would lose significantly less energy to synchrotron radiation than an electron. An accelerating relativistic charged particle emits synchrotron radiation at a rate given by [Jac99]:

$$\frac{dE}{dt} = -\frac{1}{4\pi\epsilon_0}\frac{2}{3}\frac{e^2}{m^2c^3}\left(\frac{dp_\mu}{d\tau}\frac{dp^\mu}{d\tau}\right), \tag{1.1}$$

where p^μ is the particle's four-momentum, m is its mass, τ is the proper time, e is the

[2] 760 torr = 1 atm.

elementary charge, ϵ_0 is the permittivity of free space, and c is the speed of light. If the particle accelerates without changing its direction of motion, $\left(\frac{dp_\mu}{d\tau}\frac{dp^\mu}{d\tau}\right)$ reduces to $\left(\frac{dp}{dt}\right)^2$, where t is the time in the lab frame. For a particle in a linear accelerator, Eq. 1.1 thus becomes:

$$\frac{dE}{dt} = -\frac{1}{4\pi\epsilon_0}\frac{2}{3}\frac{e^2}{m^2c^3}\left(\frac{dE}{dx}\right)^2. \tag{1.2}$$

For values of $\frac{dE}{dx}$ typical for e^+e^- colliders, this energy loss is negligible. If, however, the particle is experiencing centripetal acceleration in a circular accelerator of radius ρ, Eq. 1.1 becomes approximately [Jac99]:

$$\frac{dE}{dt} = -\frac{1}{4\pi\epsilon_0}\frac{2}{3}\frac{e^2c}{\rho^2}\beta^4\gamma^4, \tag{1.3}$$

where β is the particle's velocity in units of c, and $\gamma = 1/\sqrt{1-\beta^2}$. Since $\gamma = E/mc^2$, the rate of synchrotron radiation in this case increases inversely as the fourth power of mass. Eq. 1.3 sets a practical upper limit of about 100 GeV on the maximum energy attainable by a circular e^+e^- collider, necessitating that higher-energy e^+e^- colliders be made linear [Neu83]. In contrast, since $m_\mu/m_e \approx 200$, synchrotron radiation would be negligible in a circular $\mu^+\mu^-$ collider, allowing multi-TeV energies to be reached via relatively small accelerators.

A further advantage of the muon collider is its enhanced luminosity. A collider's event rate for a particular interaction is given in terms of the cross section σ for the interaction and the luminosity $\mathcal{L}$ of the detector as:

$$R = \mathcal{L}\sigma. \tag{1.4}$$

Since the cross sections for the interactions studied in high-energy colliders typically decrease as the square of the center-of-mass energies, luminosities of colliders must increase as the square of the collider energies to preserve event rates. Given that the luminosity of a linear collider varies approximately inversely as the classical radius of the particle being collided, and that the classical radius of the muon is 200 times smaller than that of the electron, much higher luminosities can be attained by colliding muons than by colliding electrons

[PG97]. Furthermore, since a muon collider can be made circular, its luminosity potential is also higher by a factor equal to the average number of times a muon circles the collider ring within its lifetime.

Yet another advantage of colliding muons is the increased probability of observing events involving the Higgs boson. The cross section for direct s-channel production of the Higgs boson in a collision between two identical leptons is proportional to the square of the mass of the lepton and is therefore higher by a factor of about $40,000$ in a muon collider than in an electron collider [Pal98]. Furthermore, due to the suppression in a $\mu^+\mu^-$ collider of beamstruhlung, which is the emission of synchrotron radiation by each beam at the collider's interaction point in response to the electromagnetic field of the opposite beam [B$^+$83, B$^+$89], the energy spread of the bunches can be reduced to as low as 0.003% [Pal98], which is a significant advantage for the study of narrow Higgs resonances [B$^+$95].

Although the above discussion does not nearly exhaust the $\mu^+\mu^-$ collider's advantages over the e^+e^- collider, there remain several unresolved technical problems [PG97]. One potential problem is that muons decaying within the collider ring will produce high levels of background radiation. Difficulties may also arise in the cooling of the muons, which will be discussed in the next section.

1.2 Ionization Cooling of Muons

To obtain muons, an energetic proton beam is collided into a target made of a substance with a high atomic number Z. The resulting pions then decay into muons via:

$$\pi^- \rightarrow \mu^- + \bar{\nu}_\mu \tag{1.5}$$

or the conjugate reaction. The muons produced in this way occupy a large volume in the six-dimensional phase space of generalized coordinates and momenta; to produce a collimated

beam, it is therefore necessary to cool the muons.[3]

Radiation cooling, electron cooling, and stochastic cooling, which are methods traditionally used for cooling particles, are all too slow for cooling muons, which have a relatively short lifetime of about 2 μs. A potentially feasible method is ionization cooling, where the beam is alternately passed through a dense absorber and accelerated linearly. While interactions with the electrons of the atoms in the absorber lower the momentum of a muon both longitudinally and transversely to the beam direction, the linear accelerator replenishes the lost momentum only in the longitudinal direction. The net effect is to lower the transverse momentum, as shown in Fig. 1.1. The cooling is aided by the fact that the energy a particle loses in a given thickness of absorber depends on its energy [Neu83]. Although this method cools the beam only in the transverse direction, transverse and longitudinal emittances may be exchanged by passing the beam through a bent solenoid [A$^+$99]. The cooling process may be repeated until the desired reduction in total phase-space volume is achieved.

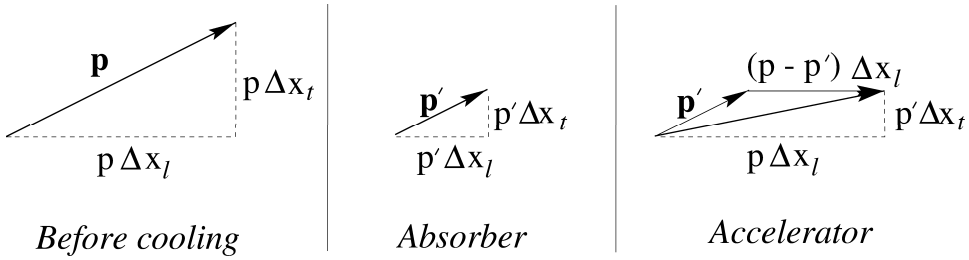

Figure 1.1: Changes in a muon's momentum as it undergoes ionization cooling. Initially, the muon has momentum $\mathbf{p}$, made up of transverse and longitudinal components $p\Delta x_t$ and $p\Delta x_l$, respectively. The effect of the absorber is to decrease the muon's momentum while preserving its direction of motion. As the accelerator stage restores only the muon's longitudinal momentum to its original value, the net effect is to decrease the transverse component of the muon's momentum.

Since the feasibility of building a muon collider will likely be determined by a demonstration of the success or failure of ionization cooling, the Muon Collider Collaboration has begun designing an experiment to test the effect of ionization cooling on the phase-space

[3] To "cool" a beam is to reduce the beam's total phase-space volume. When a beam of particles is "cooled", the "temperature" of the beam is lowered in the sense that the speeds of the component particles in the frame moving with the mean velocity of the beam are reduced. This "trajectory cooling" differs from "adiabatic cooling" which involves increasing the size of the beam [SP81].

volume of a muon bunch [A+98]. The experiment consists in measuring, before and after the cooling process, the phase-space coordinates of individual muons within an unbunched muon beam. A bunch is then artificially constructed by selecting a subset of the measurements.[4]

Fig. 1.2 shows the overall layout of the experiment, which is composed of identical measurement complexes upstream and downstream of the cooling apparatus. The quantities to be measured in each arm of the structure are the six phase-space coordinates, namely the transverse coordinates x, x', y, y', where $x' = dx/dz$ and $y' = dy/dz$; the longitudinal momentum P; and the longitudinal coordinate z, which is equivalent to the time separation of the muon from the bunch center.[5] While the first five of these coordinates may be measured to sufficient accuracy immediately before and after the cooling stage using a particle detector, the measurement of the z coordinate to the required accuracy of a few picoseconds is more involved [L+97].

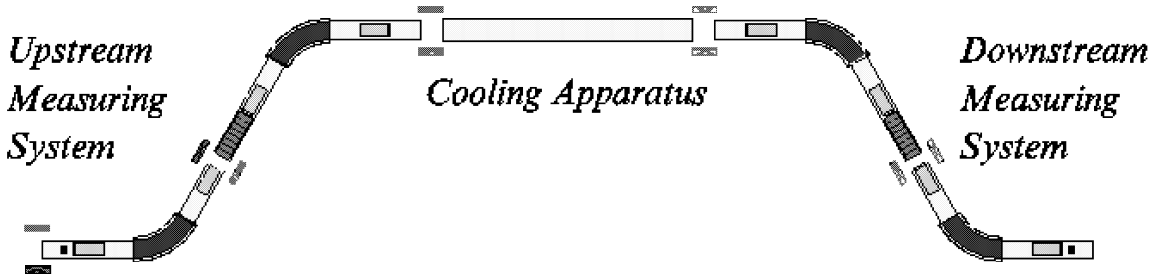

Figure 1.2: The current design of the Muon Collider Collaboration's ionization cooling experiment, as seen from above. The effect of ionization cooling on a muon bunch is determined by measuring the phase-space coordinates of individual muons before and after ionization cooling. The upstream and downstream measuring systems are each 8 m long and are encapsulated within a 3-Tesla solenoid which serves to contain and guide the muon beam. Note that the solenoid always bends in the horizontal plane.

To measure z, each muon is sent through an 800-MHz RF cavity, where it is accelerated by an amount dependent on its time of arrival with respect to the bunch center.

[4] This method of constructing a bunch does not take into account space charge: the effect on each muon of the electromagnetic field of the other muons within the bunch.

[5] The axes of the canonical phase space are the position coordinates x, y, z; and the momentum coordinates p_x, p_y, p_z. Strictly speaking, the coordinates specified here are the trace-space coordinates.

With the help of an auxiliary coarse timing measurement to resolve the ambiguity as to which quarter of the RF cycle accelerated the muon, this time-energy dependence allows the position of each muon within the selected bunch to be determined by comparing its momentum before and after the RF timing cavity.

The momentum measurement makes use of the momentum-dependence of the vertical displacement a beam undergoes as it is directed through a bent solenoid. As shown in Fig. 1.3, the beam encounters a bend in the solenoid both before and after each RF cavity; a vertical magnetic field of 0.55 T is superimposed on each bend to cancel the vertical displacement for the central beam momentum. The vertical displacement of each muon is determined by reconstructing the muon's trajectory before and after each bend in the solenoid.

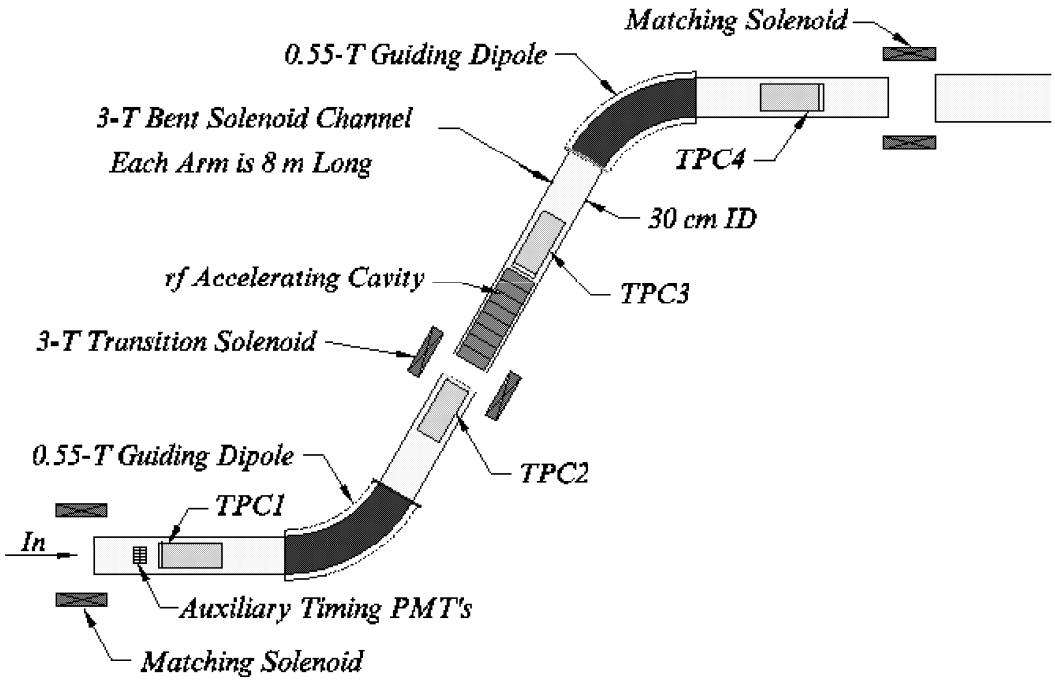

Figure 1.3: Detail of the upstream half of the structure shown in Fig. 1.2.

Given the presence of a strong magnetic field parallel to the beam direction, and the importance of minimizing the scattering of the relatively low-momentum ($100 - 300$ MeV)

muons, a low-pressure TPC is a natural choice of detector for reconstructing muon trajectories [L$^+$97]. A diagram of the TPC designed for the experiment is shown in Fig. 1.4. The TPC will be filled with methane at a pressure of 8.4 torr and a temperature of 20°C. The ionization density by minimum ionizing particles in methane at room temperature and atmospheric pressure is 25 primary clusters per cm. [Va'92], and a muon with a momentum of 165-MeV/c ionizes at a rate approximately 1.2 times the minimum [L$^+$97]. Thus, since the density of ionization in a gas is proportional to the number density of the gas, which in turn is directly proportional to the pressure and inversely proportional to the temperature, it follows that the expected ionization density at 20°C and 8.4 Torr is about 0.3 cm^{-1}. The same ionization density may be obtained by operating the chamber at 2.2 torr and 77 K, which would lower the thermal load on the solenoid's cryogenic system [L$^+$97].

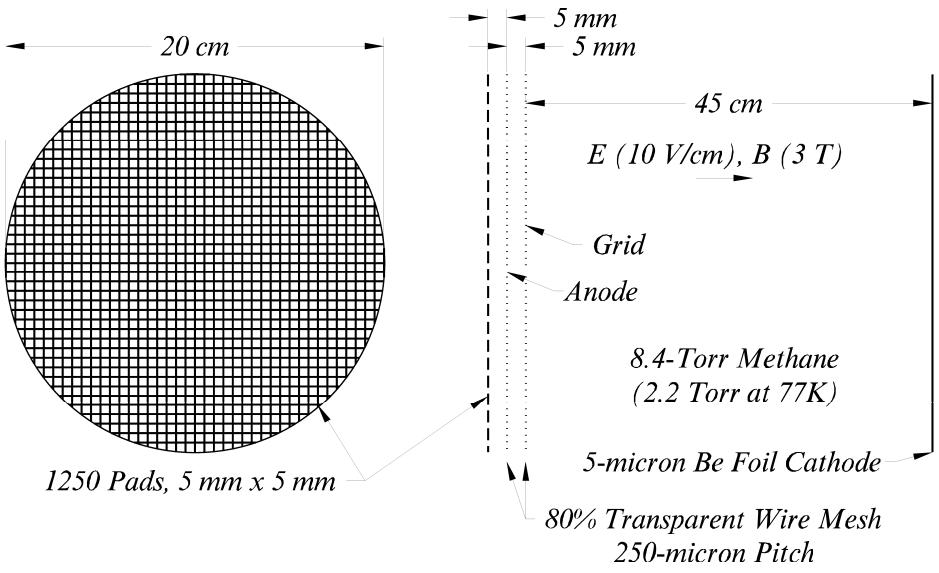

Figure 1.4: Sketch of the low-pressure TPC designed for measuring trajectories in the experiment shown in Figs. 1.2 and 1.3.

Since the drift velocity of electrons in a gas is a function of E/P, the saturation drift velocity for methane of 9×10^6 cm/s is reached at an electric field of about 10 V/cm at a pressure of 8.4 torr, and about 3 V/cm at a pressure of 2.2 torr. Thus, the low-pressure TPC will employ relatively low electric fields.

Chapter 2

The Physics of the TPC

Before the invention of the TPC in 1974 by D.R. Nygren, momentum measurements and particle identification had traditionally been performed separately in specialized detectors [MN78, MO84]. The TPC is innovative in the sense that it not only combines both functions in the same volume, but it moreover produces an intrinsically three-dimensional reconstruction of particle trajectories, which is a significant improvement over the two-dimensional readout of the traditional wire chamber.

The characteristic TPC geometry is shown in Fig. 2.1. The two main sections of the chamber are a drift volume and a detection volume, with a wire grid to separate the two regions. Since signal detection is restricted to the detection volume, the drift volume is left empty save for gas molecules. Uniform and parallel electric and magnetic fields are applied over the drift volume.

When a charged particle passes through the drift volume of a TPC, it collides with the gas molecules on its path, imparting a fraction of its energy to the molecules with which it has collided. If the energy transferred to a molecule is greater than the molecule's ionization energy, one or more electrons may be ejected. Some of these ejected electrons may themselves have sufficient energy to cause further ionization, in which case they are

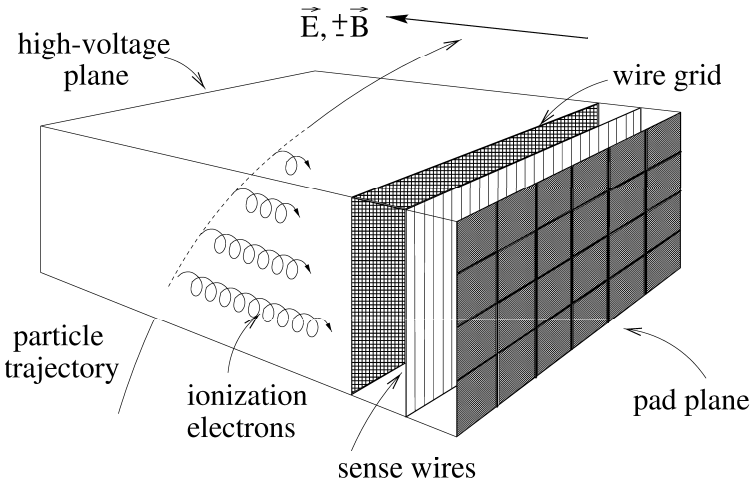

Figure 2.1: Geometry of a typical time projection chamber. Note that the radii of the helical trajectories are greatly exaggerated, and that collisions with gas molecules are not taken into account.

referred to as δ-rays. Ionization due to the original charged particle is termed primary ionization, to be distinguished from the secondary ionization caused by δ-rays [Wil50].

Whereas the ionization electrons created by the passage of a charged particle would normally recombine with their respective positive ions, the application of a sufficiently strong electric field causes them to separate from the positive ions and drift toward the detection region. The alignment of the magnetic field parallel to the electric field causes the drifting electrons to follow helical trajectories, making long drift distances possible by limiting diffusion transverse to the drift direction. This so-called helical confinement is discussed in greater detail in Chapter 3.

A drifting electron gains energy from the applied electric field but loses it on average as a result of collisions with gas molecules. The collisions provide an effective frictional force that leads to the relation:

$$\mathbf{v_d} = \mu \mathbf{E} \tag{2.1}$$

for a given gas at constant temperature and pressure, where $\mathbf{E}$ is the applied electric field, $\mathbf{v_d}$ is the constant drift velocity of the electron, and μ is the constant of proportionality known as the electron mobility [BR93].

The electric field in the drift region of the TPC is low enough that drifting ionization electrons do not pick up enough energy between collisions to cause further ionization of gas molecules. In the detection region, however, the electric field close to an anode wire is given by:

$$E = \frac{\rho}{2\pi\epsilon_0}\frac{1}{r}, \tag{2.2}$$

where ρ is the linear charge density on the wire, r is the radial distance from the wire, and ϵ_0 is the permittivity of free space. An electron approaching a wire therefore travels in an increasing electric field. Since an electron drifting with a mean free path of λ picks up an average energy $eE\lambda$ between collisions, it becomes increasingly energetic as it approaches a wire, eventually crossing the threshold of ionization and ionizing another gas molecule. The ionized electron in turn is accelerated by the electric field and causes additional ionization. This multiplication process, which is referred to as a Townsend avalanche, facilitates the observation of small signals in detectors by increasing the signal-to-noise ratio. The number of ionization electrons increases according to the Townsend equation:

$$\frac{dn}{dx} = \alpha\, n, \tag{2.3}$$

where α is the first Townsend coefficient for the gas, and generally increases with increasing field strength beyond the threshold of ionization, which is typically of the order of 10^6V/m in most gases at atmospheric pressure [Kno79].

In a time-projection chamber, the avalanche is detected not by the signal induced on the anode wires but the image charge induced on the cathode plane behind the anode wires. By segmenting the cathode plane into pads and finding the center-of-gravity of the collected charge, two orthogonal coordinates of the initial ionization on a plane perpendicular to the drift field may be obtained with high precision. Furthermore, since the drift velocity of the ionization electrons is constant, the coordinate parallel to the electric field may be deduced from the arrival time of the signals, provided that the time of incidence of the charged particle is known. In this way, the three-dimensional trajectory of the ionizing particle may be reconstructed.

2.1 Momentum Measurement

Once the trajectory of a charged particle has been reconstructed, the measurement of its momentum is relatively straightforward. The momentum of a particle of charge q moving in a magnetic field of magnitude B is given by:

$$p\cos\theta = qBr, \tag{2.4}$$

where θ is the pitch angle, and r is the radius of curvature of the particle's trajectory. The momentum of the ionizing particle can thus be determined by measuring the pitch angle and radius of curvature of the reconstructed trajectory.

2.2 Particle Identification

If the TPC is operated in the proportional mode, where the gain is low enough that the ionization energy collected at the anode wires is proportional to the primary ionization, the total amount of charge collected may be used to identify the charged particle that produced the ionization. The mean rate of energy loss due to ionization per unit length traveled by a particle of unit elementary charge is given by the Bethe-Bloch formula [C$^+$98]:

$$\frac{dE}{dx} = -\frac{K}{A}\,Z\,\frac{1}{\beta^2}\left[\frac{1}{2}\ln\frac{2m_e c^2\beta^2\gamma^2 T_{\max}}{I^2} - \beta^2 - \frac{\delta}{2}\right], \tag{2.5}$$

where $K/A = 0.307$ MeV g^{-1}cm^2, Z is the atomic number of the medium, I is the mean excitation energy, $T_{\max}$ is the maximum kinetic energy which a free electron can gain in a single collision, δ is a correction constant, and m_e is the electron mass. At low energies, the energy loss is proportional to $1/\beta^2$. The Bethe-Bloch formula relates the energy deposited by the particle to its velocity, which, when combined with the momentum information from the reconstructed trajectory, reveals the identity of the ionizing particle. Fig. 2.2 shows measurements of ionization energy loss obtained with the PEP4/9-TPC. The particle-ID

function of the TPC will not be used in the low-pressure TPC for the ionization cooling experiment.

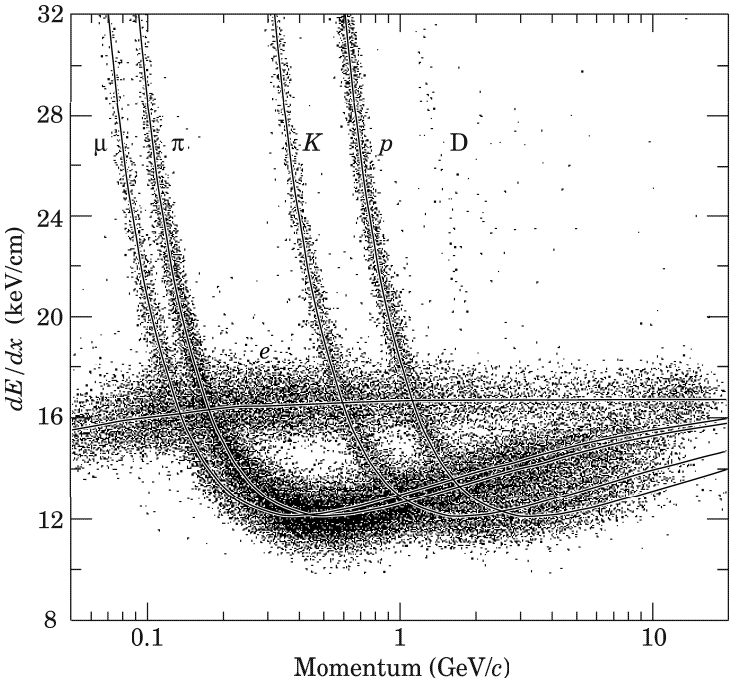

Figure 2.2: The rate of energy loss per distance travelled as measured by the PEP4/9-TPC. From Ref. [C+98].

Chapter 3

Diffusion

In a time-projection chamber, the parallel alignment of the electric and magnetic fields makes long drift distances possible by substantially reducing the transverse diffusion of ionization electrons. The next two sections detail the derivation of diffusion outlined in Ref. [PEP76]. Section 3.3 presents estimates of the resolution of the low-pressure TPC, both with and without a magnetic field.

3.1 The Case of Zero Magnetic Field

An ideal, point-like cloud of electrons that is initially located at the origin and begins at time $t = 0$ to drift in the z direction with a drift velocity v_d will, if the diffusion has no preferred direction, form a Gaussian density distribution described at time t as:

$$n = \left(\frac{1}{\sqrt{4\pi Dt}}\right)^3 \exp\left(-\frac{r^2}{4Dt}\right), \tag{3.1}$$

where $r^2 = x^2 + y^2 + (z - v_d t)^2$, and D is the diffusion constant. [BR93]. The width of the Gaussian is:

$$\sigma = \sqrt{2Dt}. \tag{3.2}$$

By considering the collisions between the electrons and the gas molecules, the width of the Gaussian distribution in a given direction may also be expressed in terms of the mean free path λ and the mean collision time τ as [BR93]:

$$\sigma^2 = \frac{2}{3}\frac{\lambda^2}{\tau}t, \tag{3.3}$$

which, when combined with Eq. 3.2, gives:

$$D = \frac{\lambda^2}{3\tau}. \tag{3.4}$$

Eq. 3.4 may be expressed as:

$$D = \frac{v^2\tau}{3} = \frac{2}{3}\frac{\varepsilon}{m_e}\tau = \frac{2}{3}\frac{\varepsilon}{e}\mu = \frac{2}{3}\frac{\varepsilon}{e}\frac{v_d}{E}, \tag{3.5}$$

where $v = \lambda/\tau$ is the mean electron velocity between collisions (to be distinguished from the drift velocity v_d), $\varepsilon = m_e v^2/2$ is the electron energy, and $\mu = e\tau/m_e = v_d/E$ is the electron mobility.

If it is assumed that the electron energy due to the electric field is negligible, and that ε is accordingly dominated by the thermal energy of the electron cloud $\varepsilon = \frac{3}{2}kT$, Eq. 3.5 becomes:

$$D = \frac{kT}{e}\frac{v_d}{E}, \tag{3.6}$$

which is known as the Nernst-Townsend or Einstein relation for isotropic diffusion. In most drift chambers, the energy that an electron gains from the electric field is much larger than its thermal energy, and this assumption may not be made [BR93].

Expressing the drift time t in terms of the total drift distance L as $D = L/v_d$, and using $t = \frac{v^2\tau}{3}$, Eq.3.2 may be written:

$$\sigma = \sqrt{\frac{2}{3}v\lambda\frac{L}{v_d}}, \tag{3.7}$$

which shows that in the absence of a magnetic field, diffusion grows as the square of the mean free path. By successively eliminating v_d, λ, v^2, and finally μ with the help of the

relations used to construct Eq. 3.5, Eq. 3.7 gives:

$$\sigma = \sqrt{\frac{4}{3}\,\varepsilon\,\frac{L}{E}}. \tag{3.8}$$

Thus, for a given ratio of the electric field to the pressure E/P at a constant value of ε,

$$\sigma \propto \sqrt{\frac{L}{P}}. \tag{3.9}$$

Eq. 3.8 is used in Section 3.3 to estimate the resolution of the low-pressure TPC.

3.2 Diffusion in the Presence of a Magnetic Field

The situation is considerably different when diffusion occurs under a uniform magnetic field. An electron moving with a momentum component perpendicular to a uniform magnetic field follows a helical trajectory about an axis parallel to the direction of the magnetic field, with a radius given by:

$$r = \frac{v}{\omega}\sin\theta, \tag{3.10}$$

where v is the electron's velocity, θ is the angle between its velocity vector and the magnetic field lines, and $\omega = Be/m_e$ is the cyclotron frequency. Thus, by making B large enough that the radius of curvature of the electrons is small relative to the mean free path, diffusion may be suppressed. Fig. 3.1 shows the decrease in transverse diffusion as the strength of the magnetic field is increased.

The diffusion constant for diffusion transverse to the magnetic-field direction is given by [BR93]:

$$D(B) = \frac{D(0)}{1+\omega^2\tau^2}. \tag{3.11}$$

Inserting this into Eq. 3.2 and considering the case of a large magnetic field with $\omega\tau \gg 1$ gives:

$$\sigma = \sqrt{\frac{2Dt}{\omega^2\tau^2}} = \sqrt{\frac{2}{\omega^2\tau^2}\,D\,\frac{L}{v_d}} = \sqrt{\frac{2}{\omega^2}\,\frac{v^3}{3\lambda}\,\frac{L}{v_d}}. \tag{3.12}$$

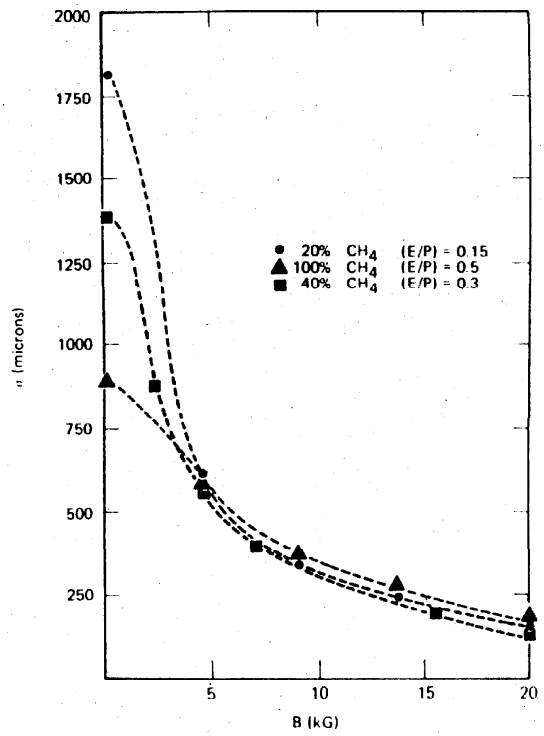

Figure 3.1: Transverse diffusion in μm, versus the applied magnetic field in kG, for different ratios of argon and methane in the PEP4 TPC. From Ref. [PEP76].

Comparing Eq. 3.7 and Eq. 3.12 reveals not only that diffusion is suppressed for strong magnetic fields, but that for constant drift length L and drift velocity v_d, diffusion is proportional to $\sqrt{v\lambda}$ in the absence of a magnetic field, and to $\sqrt{v^3/\lambda}$ in a strong magnetic field. Thus, a strong magnetic field makes the transverse diffusion more sensitively dependent on electron energy, while reversing the dependence on λ; whereas in a strong magnetic field the resolution improves as λ increases, in the absence of a magnetic field the resolution deteriorates as λ becomes longer. Furthermore, since low electrics field correspond to small values of v_d while high electric fields correspond to large values of v, a minimum σ should be attained at some value of the drift field [PEP76].

Eq. 3.12 may be simplified as:

$$\sigma = \sqrt{\frac{2}{3}\frac{v^2}{\omega^2}\frac{1}{\tau}\frac{L}{v_d}} = \sqrt{\frac{2}{3}\frac{v^2}{\omega^2}\frac{e}{m_e\mu}\frac{L}{v_d}} = \sqrt{\frac{2}{3}\frac{v^2}{\omega^2}\frac{e}{m_e}\frac{EL}{v_d^2}} = \sqrt{\frac{4}{3}\frac{\varepsilon}{m_e^2\omega^2}\frac{eEL}{v_d^2}}, \qquad (3.13)$$

which shows that for constant E/P, ε, v_d and ω,

$$\sigma \propto \sqrt{LP}. \tag{3.14}$$

Comparing Eq. 3.9 and Eq. 3.14 makes it clear that although decreasing pressure deteriorates the resolution in the absence of a magnetic field, it improves the resolution in a strong magnetic field.

The inverse dependence of the diffusion on the mean free path λ in Eq. 3.12 indicates that the transverse resolution of the TPC may also be aided by the Ramsauer-Townsend effect. This effect is a purely quantum-mechanical phenomenon responsible for the dependence of an electron's mean free path in a gas on the electron's energy. The dependence is shown in Fig. 3.2 for argon and methane, where there is a deep minimum in the cross section for collisions between electrons and gas atoms at electron energies of about 1/3 eV. At such low energies, the de Broglie wavelength of an electron becomes comparable to the size of the gas atoms, which as a result effectively become invisible to the electron. This effect is significant for noble gases and simple molecules like methane, the shell structure of which is similar to that of neon [vE65]. Thus, if a methane-TPC is operated close to the minimum of the methane curve in Fig. 3.2, the increased mean free path would contribute to the decrease in diffusion, as indicated by Eq. 3.12. A rough estimate of the electron energies presented in the next section indicates that while operating the TPC at room temperature with pressures of 8.4 torr, 20 torr or 1 atm minimize the collision cross section, operating the TPC at $P = 2.2$ torr with $T = 77$ K produces electron energies that are much lower than the energy corresponding to the minimum collision cross section.

Although diffusion along the longitudinal direction is not affected by the presence of a B field, it has been noted that diffusion longitudinal and transverse to a uniform electric field in the absence of a magnetic field are not necessarily equivalent. In particular, in argon, the ratio between longitudinal and transverse diffusion may be as low as about 1/7 [PL69a, PL69b]. Since there is a possibility that such effects may become important in the operation regime of the low-pressure TPC, this phenomenon needs to be better understood.

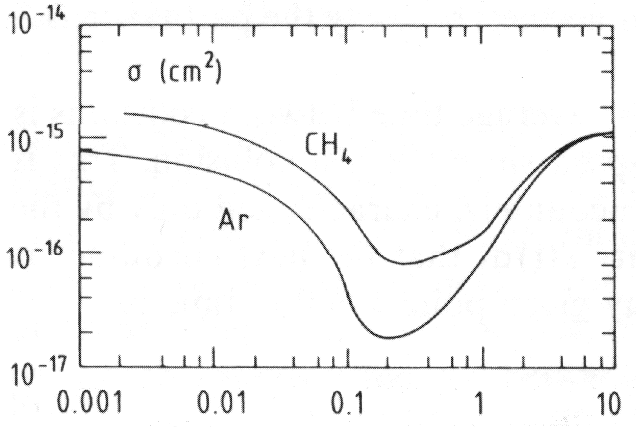

Figure 3.2: Dependence of collision cross section on electron energy for methane and argon. The vertical axis represents the collision cross section in cm^2, and the horizontal axis represents electron energy in eV. Taken from Ref. [BR93]; originally from Ref. [Sch86].

3.3 Estimates of Diffusion for the Low-Pressure TPC

This section presents diffusion estimates for operating the TPC with $B = 0$ and $B = 3$ T, (a) at $T = 77$ K and $P = 2.2$ torr; (b) at $T = 20°$C and $P = 8.4$ torr; (c) at $T = 20°$C and $P = 20$ torr, and (d) at $T = 20°$C and $P = 1$ atm.

Before examining the diffusion, a rough estimate of the electron energy was made in order to determine the applicability of the approximation $\varepsilon = \varepsilon_E + \frac{3}{2}kT \approx \frac{3}{2}kT$. The electron energy was estimated using the collision cross section of electrons in methane given by Fig. 3.2. Starting from the energy corresponding to the minimum of the collision cross section, a preliminary estimate of the mean free path was made using:

$$\lambda = \frac{1}{n\,\sigma_{\text{coll}}}, \tag{3.15}$$

where n is the number density of the gas molecules, and σ_{coll} is the cross section for the collision of electrons with methane molecules. The corresponding electron energy $\varepsilon = e\lambda E + \frac{3}{2}kT$ was then calculated. Depending on whether the calculated energy was higher or lower than the initial estimate, a new estimate was made, and the process was repeated until ε converged. As shown in Table 3.1, the energy due to the electric field was found to

	(a)	(b)	(c)	(d)
Temperature (K)	77	293	293	293
Pressure (torr)	2.2	8.4	20	760
Electric Field Strength (V/cm)	2.6	10	24	900
Density (cm^{-3})	2.7×10^{17}	2.7×10^{17}	6.5×10^{17}	2.5×10^{19}
$\varepsilon_{\mathrm{thermal}} = \frac{3}{2}kT$ (eV)	0.01	0.04	0.04	0.04
ε (eV)	0.01	0.4	0.4	0.4
$\sigma_l/\sqrt{L}$ ($\mathrm{cm}^{1/2}$)	7.1×10^{-2}	0.23	0.15	0.024
$\sigma_t/\sqrt{L}$ ($\mathrm{cm}^{1/2}$)	6.88×10^{-5}	8.5×10^{-4}	1.32×10^{-3}	8.1×10^{-3}

Table 3.1: Values of various quantities calculated for different values of temperature and pressure.

dominate in all cases but case (a), where $T = 77$ K.

Assuming that longitudinal diffusion is the same as transverse diffusion in the absence of a magnetic field, the longitudinal diffusion was estimated using Eq. 3.8. The transverse diffusion in a magnetic field of 3 T was then estimated using Eq. 3.13. The results are shown in Table 3.1. According to these estimates, the over a drift length of 45 cm is 57 μm at $P = 8.4$ Torr and $T = 20°$C, and 4.6 μm at $P = 2.2$ Torr and $T = 77$K, much lower than the expected electronic resolution.

The estimate of longitudinal diffusion for $P = 1$ atm and $T = 20°$C is 0.024 $\mathrm{cm}^{1/2}$, somewhat larger than but comparable to the diffusion obtained by Palladino and Sadoulet to be 0.013 $\mathrm{cm}^{1/2}$, as shown in Fig. 3.4.

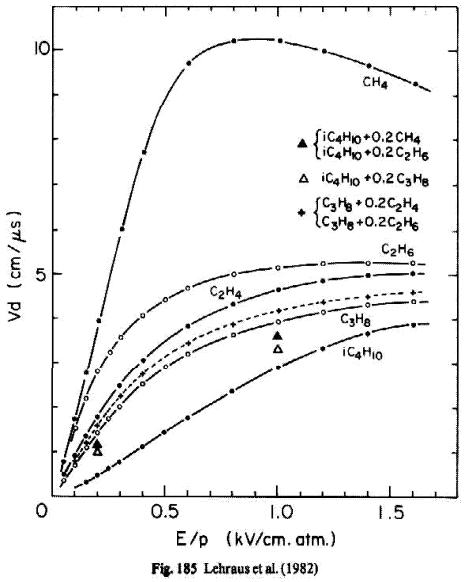

Figure 3.3: Drift velocity of pure hydrocarbons at atmospheric pressure. From Ref. [ILT82].

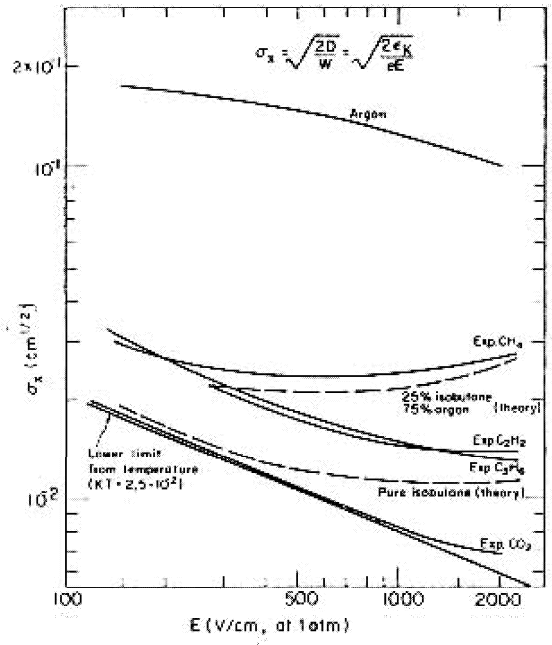

Figure 3.4: $\sigma_l/\sqrt{L}$ for several gases, including pure methane at atmospheric pressure and room temperature. From Ref. [PS75].

Chapter 4

The Low-Pressure TPC Prototype

The TPC prototype will be operated in a magnet which can produce fields of up to 6.5 T, uniform to within 1% over a distance of about 9 cm [Pre98]. Because of the small range of the magnet's optimum field, and the small diameter of the magnet's warm bore where the TPC will be placed, the size of the chamber must necessarily be small. Fig. 4.1 shows the sizes of the warm-bore magnet and the vacuum vessel used for pumping down the chamber and filling it with gas at low pressures.

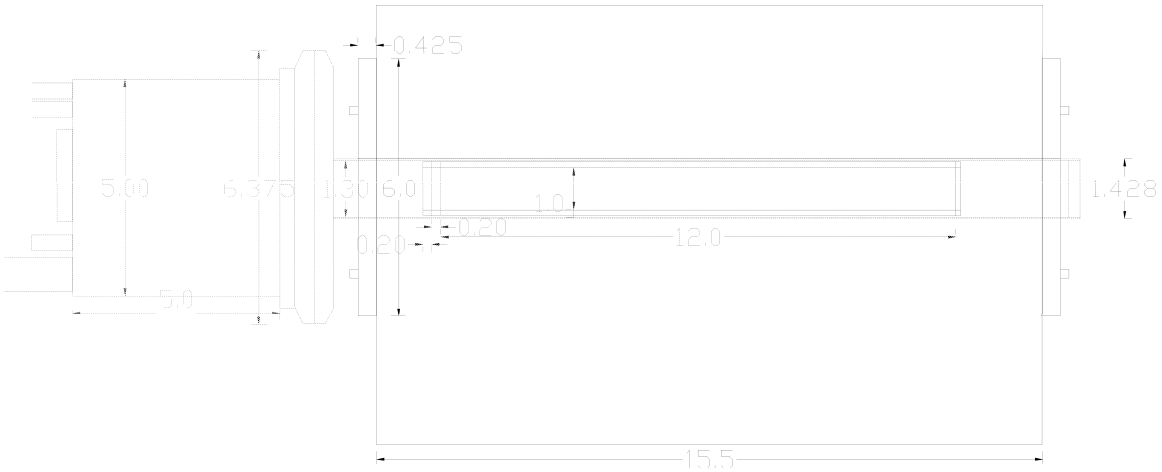

Figure 4.1: The vacuum vessel is shown inside the warm-bore magnet. The TPC prototype is placed in the narrow section of the vessel. Sizes are given in units of inches.

A diagram of the low-pressure TPC prototype is shown in Fig. 4.2. Due to the small size of the chamber, the drift field is produced not by a set of conductive rings connected by series resistors as is usually done, but by applying a voltage gradient accross a layer of carbon-loaded kapton film with a resistivity of approximately 1.4 MΩ/□, which is glued to the walls of the drift volume. The uniformity of the film's resistivity was measured and reported in Ref. [Gul98].

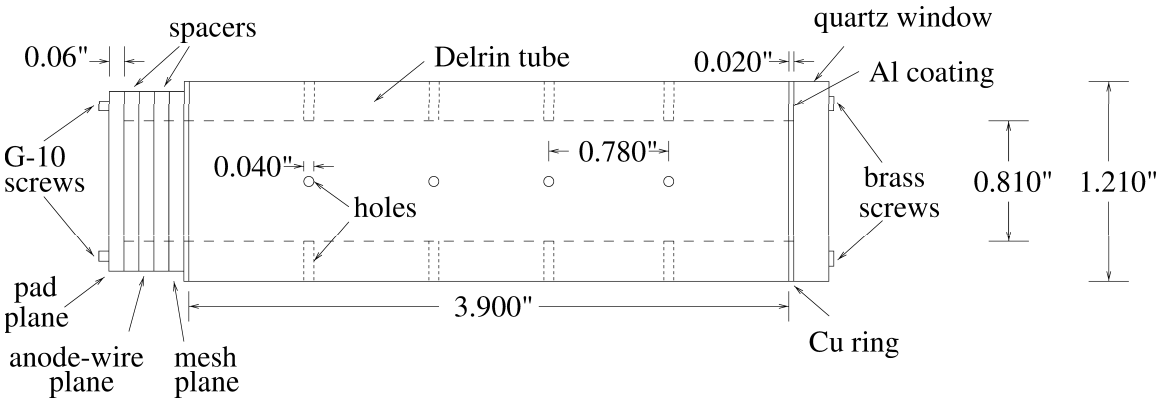

Figure 4.2: A two-dimensional diagram of the cylindrical low-pressure TPC prototype.

In preparing the drift volume, care was taken to ensure that the kapton film would lie flat against the walls of the drift volume and would be undisturbed by the pumping of gas into and out of the chamber. Accordingly, sixteen holes were drilled through the delrin cylinder, half of which were left empty to allow gas to pass through. The rest of the holes were filled with a small amount of glue to affix the film to the delrin. Excess film, cut into narrow strips, was left at the ends of the tube, folded over the edge, and glued to the delrin. To guarantee contact between the copper rings and the film, the ends of the tube were covered with silver epoxy before attaching the copper rings.

The end of the chamber opposite from the detection region is composed of a quartz window coated with aluminum to provide photoelectrons for testing the chamber. The detection end consists of a mesh plane, an anode-wire plane, and a pad plane, held apart by three circular spacers. A diagram of the rings used for the detection planes is shown in Fig. 4.3. The drift field is produced by grounding the quartz window and applying a voltage

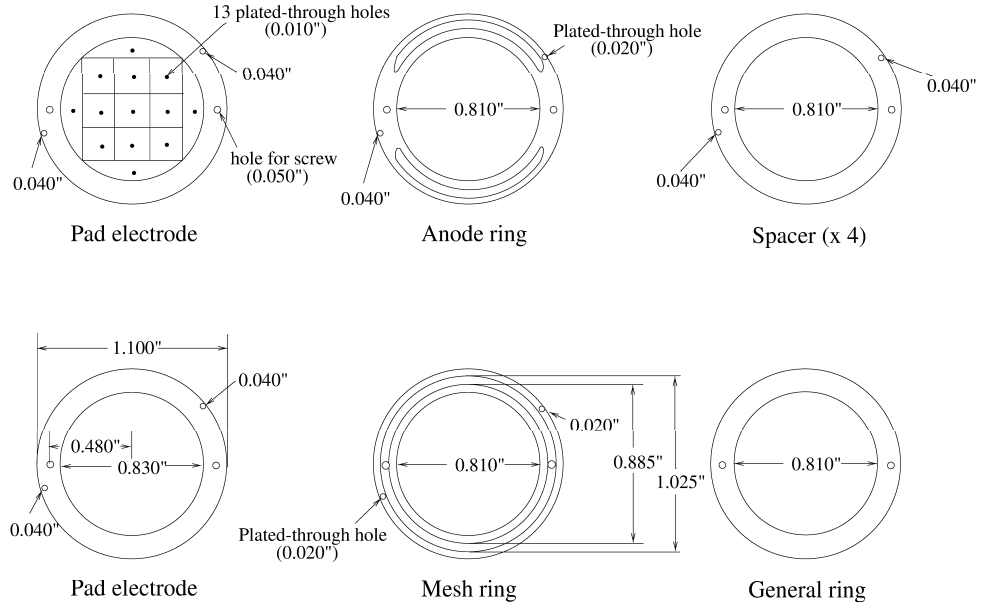

Figure 4.3: The detection rings used in the detection region of the TPC prototype. The anode ring and the mesh ring have copper-coated regions for soldering anode wires and steel mesh. Each ring is made of 0.06″-thick G-10 board.

to the mesh plane.

The small size of the chamber presented challenging sparking problems when the voltage on the anode wires was increased. In the initial design of the chamber, the outer diameter of the detection rings was equal to the outer diameter of the drift tube, and several layers of mylar were used to separate the detection region from the grounded walls of the vacuum vessel. It was found that when a high voltage was applied to the anode-wire plane, the presence, despite the mylar, of low-pressure gas in the small space between the anode-wire frame and the grounded walls of the vacuum vessel, where the voltage gradient was very high, caused sparking between the rings and the vacuum vessel. In addition, the initial design had a larger inner diameter for the detection rings and consequently a smaller ring area, which caused sparks to occur frequently between the detection planes. To reduce the sparking, the design of the chamber was revised, increasing the space between the detection planes and the walls of the vacuum vessel. The inner diameter was also decreased in order to reduce the fraction of the ring area covered by solder.

Chapter 5

Measurements of Resolution

This chapter describes the measurement of the longitudinal resolution of the low-pressure TPC prototype at zero magnetic field. The measurement is performed by focusing a laser beam at the center of the aluminum-coated window of the TPC and measuring the drift times of photoelectrons released from the aluminum.

5.1 Experimental Setup

It is essential for the measurement that only signals induced by single photoelectrons be recorded, since a signal induced by more than one photoelectron may distort the measured resolution. The probability of observing multi-photoelectron events may be estimated by using the Poisson distribution:

$$f(r;\mu) = \frac{\mu^r e^{-\mu}}{r\,!}\,, \tag{5.1}$$

where f is the probability that exactly r events will occur in a given interval, if the events occur independently of one another and of the interval, at an average rate of μ per interval [C$^+$98]. Letting μ equal the average number of events per trigger, and r the number of single-photoelectron events in one trigger, the probability that two single-photoelectron

events are recorded within one trigger is found to be 0.4% when $\mu = 0.1$, and 1.6% when $\mu = 0.2$. The probability of observing multi-photoelectron events may therefore be lowered to a negligible level by attenuating the incident laser beam to ensure an event-to-trigger ratio of approximately 0.1.

One complication is that even when the event-to-trigger ratio is low, multiple-photoelectron events may be recorded if the voltage on the anode wires is so low that single-photoelectron events do not generate a signal larger than the electronic noise. In this case, the longitudinal diffusion would be underestimated. To prevent this scenario as much as possible, the chamber was operated at the maximum voltage where the signal was not dominated by secondary avalanches.[1]

The setup used for determining the maximum voltage for making the timing measurement is outlined in Fig. 5.1. A deuterium UV lamp was shined toward the aluminum-coated window of the TPC. The signal from the pad plane was amplified first in a charge-sensitive ORTEC 142PC preamplifier, and then in an ORTEC 570 amplifier, the output of which was recorded on a multi-channel analyzer calibrated to record the total charge induced on the pad in units of electrons. The anode-wire voltage was supplied by a BERTAN 277X high-voltage supply, while the mesh and pad voltages were supplied by a BERTAN 1755 high voltage power supply. Keeping the pad voltage approximately 100 V higher than the mesh voltage in order to suppress signals created by photoelectrons released from the pad plane, the anode-wire voltage was increased in steps of 50 V, and the observed signals were used to determine the highest anode-wire voltage that could be reached before secondary avalanches began.

Fig. 5.2 shows the experimental setup used for measuring the drift velocities and longitudinal resolution for single-photoelectron events with the TPC prototype. In this case, the beam from a Laser Photonics LN203C pulsed nitrogen laser was focused on the aluminum-

[1] A secondary avalanche, as the name implies, refers to a second avalanche formed when an energetic photon produced in the original avalanche travels radially a distance larger than the size of the original avalanche and ionizes a gas molecule [BR93].

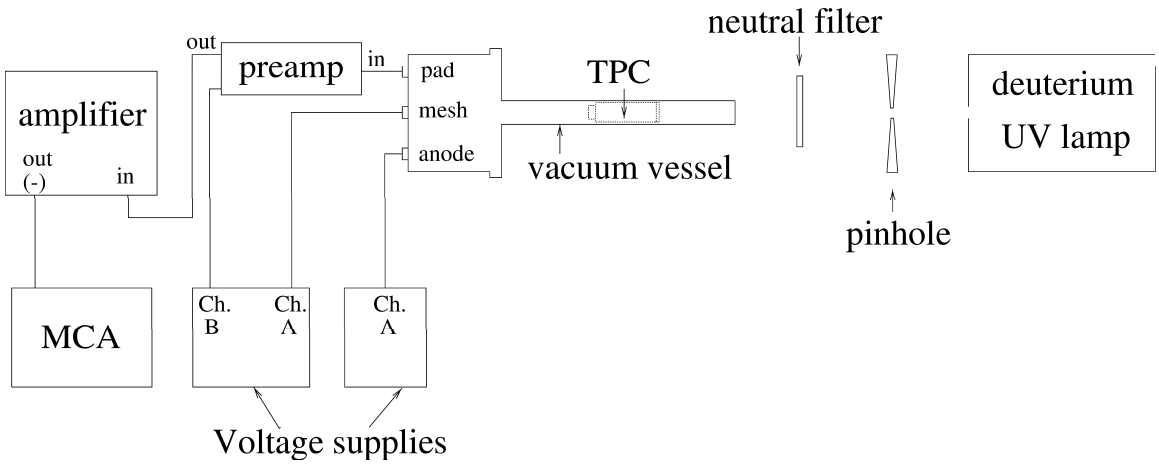

Figure 5.1: Experimental setup used for determining the maximum voltage at which the chamber could be operated without inducing secondary avalanches.

coated window of the TPC. The pad signal was then passed through a LeCroy TRA402TB preamplifier, which is a current-to-voltage converting fast transresistance amplifier. The signal from the preeamplifier was fed directly into a LeCroy 623B discriminator, the output of which provided the stop signal for the CANBERRA model 2145 time-to-amplitude converter (TAC). The start signal for the TAC was obtained by splitting the laser beam and directing it toward a photodiode as shown in Fig. 5.2, and passing the resulting signal through the LeCroy 623B discriminator. The trigger signal obtained in this way was also fed into a TENNELEC TC 536 counter and timer to keep track of the trigger rate. In some of the measurements, where it was necessary to reject noise from the laser, the trigger signal was delayed by 0.3 μs using a Phillips model 794 gate/delay generator before being sent into the TAC start input. The output of the TAC was then analyzed on a multi-channel analyzer calibrated with the TAC to give the time between the TAC start and stop signals.

5.2 Results

The experimental setup described in the previous section was used to record the drift time of laser-induced photoelectrons with methane, ethane and isobutane at several values

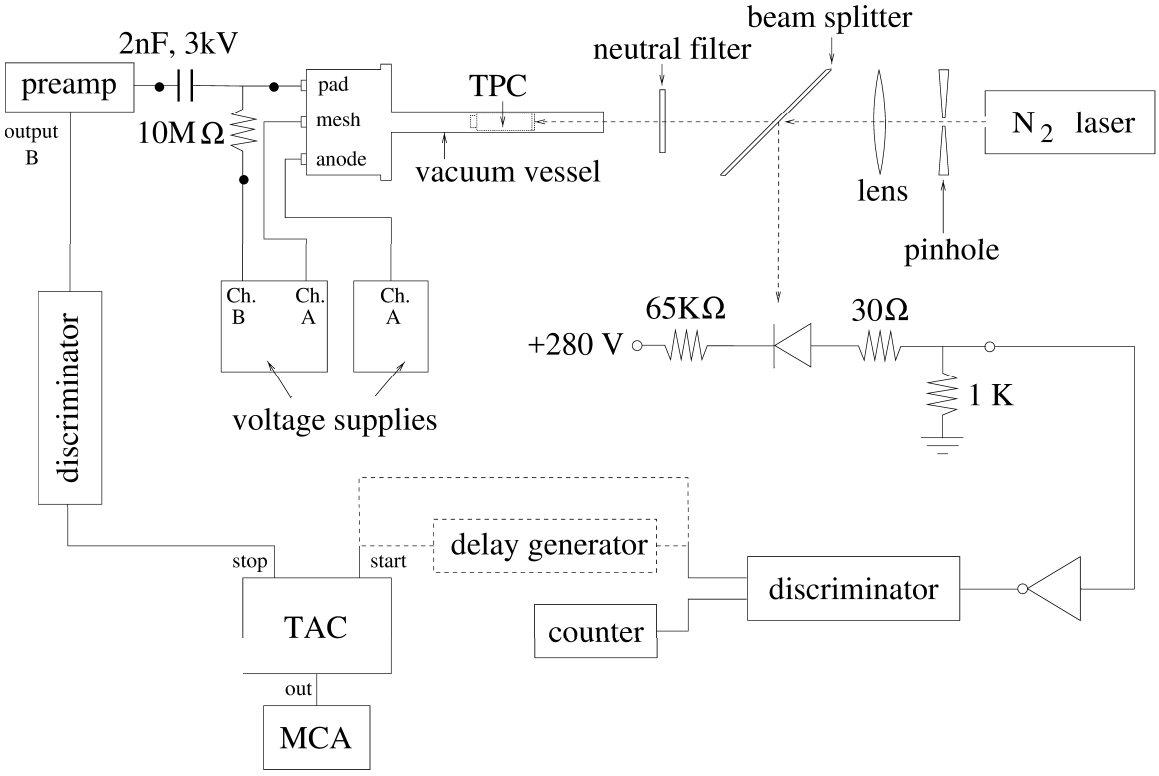

Figure 5.2: Experimental setup used for measuring the drift velocity and longitudinal resolution for single-photoelectron events observed with the low-pressure TPC prototype.

of gas pressure P and drift electric field E. About 1000 events on average were recorded for each combination of E and P. The distribution of drift times obtained in each case with the multi-channel analyzer was fit to a Gaussian. The drift velocity was computed from the mean of the Gaussian x as the ratio of the total drift distance to the drift time:

$$v_d = \frac{10\text{cm}}{x} \,. \tag{5.2}$$

The longitudinal resolution was then computed from the standard deviation σ_x of the Gaussian as:

$$\sigma_z = \sigma_x \, v_d \,. \tag{5.3}$$

The results for methane, ethane and isobutane are shown in Figs. 5.3, 5.4, and 5.5, respectively.

As indicated in the figures, the drift velocities obtained for methane and ethane at

low pressure are in reasonable agreement with the data obtained by Lehraus et al., which was shown in Fig. 3.3. The diffusion measurement for methane, however, agrees with data previously recorded at atmospheric pressure only for very low values of E/P. While the atmospheric-pressure data indicates an increase in diffusion at values of E/P above approximately 0.4 V cm^{-1} torr^{-1}, the diffusion that has been measured with the TPC prototype continues to decrease over the range of E/P measured, up to about 2 V cm^{-1} torr^{-1}. No recorded diffusion data for ethane, isobutane, or low-pressure methane has been found to provide a comparison.

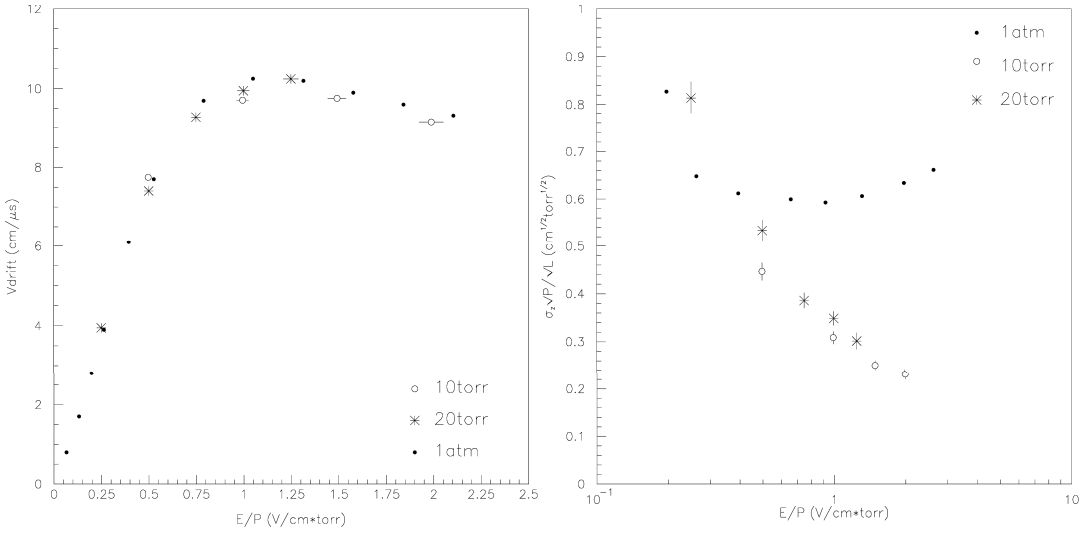

Figure 5.3: Drift velocities (left) and longitudinal resolution (right) measured with methane at $P = 10$ torr and $P = 20$ torr. The anode-wire voltage was 870 V and 1050 V above the pad and mesh voltages for $P = 10$ torr and $P = 20$ torr, respectively. Drift velocity values recorded by Lehraus et al. [ILT82], and diffusion measurements recorded by E. Barrelet et al. [ea82] for methane at atmospheric pressure are also indicated.

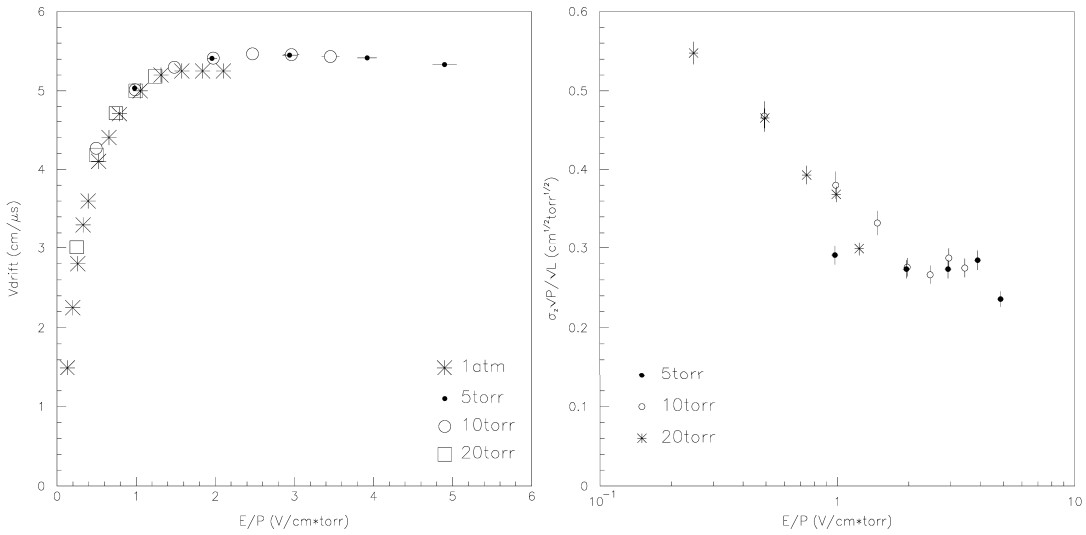

Figure 5.4: Drift velocities (left) and longitudinal resolution (right) measured with ethane at $P = 5$ torr, $P = 10$ torr, and $P = 20$ torr. The anode-wire voltage was 710 V, 800 V, and 975 V above the pad and mesh voltages for $P = 5$ torr, $P = 10$ torr, and $P = 20$ torr, respectively. Drift velocity values recorded by Lehraus et al. for ethane at atmospheric pressure are also indicated.

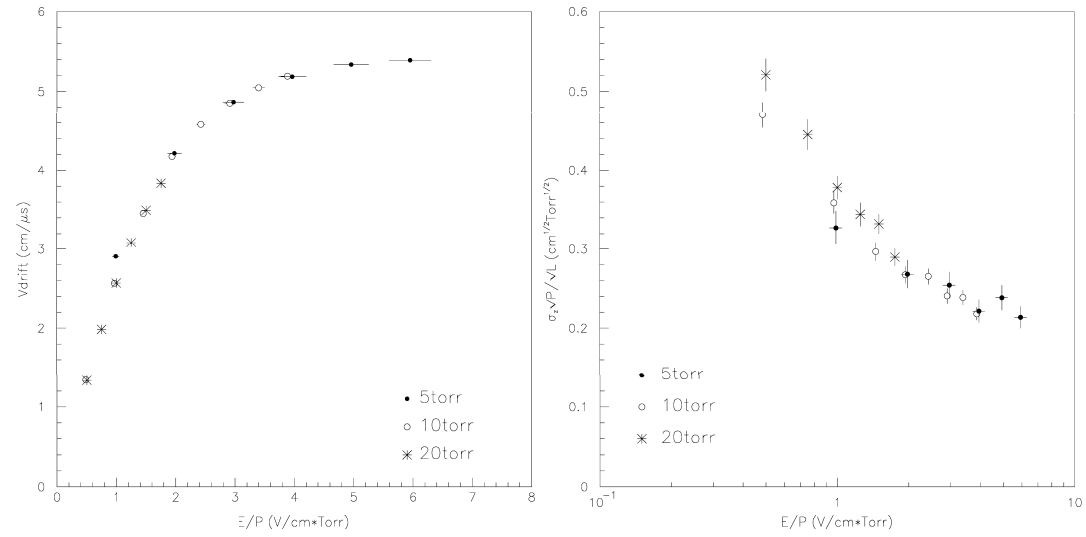

Figure 5.5: Drift velocities (left) and longitudinal resolution (right) measured with isobutane at $P = 5$ torr, $P = 10$ torr, and $P = 20$ torr. The anode-wire voltage was 720 V, 870 V, and 1140 V above the mesh voltage for $P = 5$ torr, $P = 10$ torr, and $P = 20$ torr, respectively. The pad voltage was kept 150 V above the mesh voltage for $P = 5$ torr, and 100 V above the mesh voltage for $P = 10$ torr and $P = 20$ torr.

Chapter 6

Conclusion

Since the longitudinal-resolution data obtained for methane with the low-pressure TPC prototype disagrees at high values of E/V with data that has been previously published using methane at atmospheric pressure, further testing is required in order to determine whether the discrepancy is caused by a measurement error, or by a low-pressure effect as yet undiscovered. One way of testing the validity of the observed data would be to use the TPC to measure the diffusion at atmospheric pressures and compare the results with the published data. This is not feasible, however, as the low-pressure TPC prototype cannot be operated at pressures above 50 torr. A new chamber is therefore being built, which will be functional at both atmospheric and low pressures. This will not only provide an independent test of the data obtained with the TPC, but it will also allow the measurement of the longitudinal diffusion as a function of pressure.

Meanwhile, a readout system for the pad signals is being developed using the front-end electronics (FEE) card of the STAR TPC which is being built for the Relativistic Heavy Ion Collider (RHIC) [K^+]. Transverse diffusion in the low-pressure TPC prototype is expected to be measured as a function of applied magnetic field in the near future.

Bibliography

[A+98] C.M. Ankenbrandt et al. Ionization cooling research and development program for a high luminosity muon collider. FNAL Proposal P904, http://www.fnal.gov/projects/muon_collider/cool/proposal/proposal.html, April 1998.

[A+99] C.M. Ankenbrandt et al. Status of muon collider research and development and future plans. BNL-65623, Fermilab-PUB-98/179, LBNL-41935, http://www.cap.bnl.gov/mumu/status_report.html, January 1999.

[B+83] M. Bassetti et al. Properties and possible use of beam-beam synchrotron radiation. *IEEE Trans. Nucl. Sci.*, NS-30(4):2182–2184, August 1983.

[B+89] G. Bonvicini et al. First observation of beamstrahlung. *Phys. Rev. Lett*, 62(20):2381–2384, May 1989.

[B+95] V. Barger et al. s-channel higgs boson production at a muon collider. *Phys. Rev. Lett.*, 75(8):1462–1465, August 1995.

[BR93] Walter Blum and Luigi Rolandi. *Particle Detection with Drift Chambers.* Springer-Verlag, Berlin, 1993.

[C+98] C. Caso et al. Review of particle physics. Springer-Verlag, 1998. Eur. Phys. J. C, Vol.3, No.1-4.

[ea82] E. Barrelet et al. In J. Fehlmann and G. Viertel, editor, *Compilation of Data for Drift Chamber Operation*, 1982. CERN-EP 82-09.

[Gul98] Hulya Guler. Properties of high-resistivity carbon-loaded kapton. Princeton/$\mu\mu$/**98-14**,http://viper.princeton.edu/~hulya/ph/tpc/field/film/film/film.ps, November 1998.

[ILT82] R. Matthewson I. Lehraus and W. Tejessy. dE/dx measurements in Ne, Ar, Kr, Xe and pure hydrocarbons. *Nucl. Instr. and Meth.*, 200:199–210, 1982.

[Jac99] John D. Jackson. *Classical Electrodynamics.* John Wiley & Sons, New York, 3rd edition, 1999.

[K$^+$] S.R. Klein et al. Front end electronics for the STAR TPC. http://rsgi01.rhic.bnl.gov/star/starlib/doc/www/sno/ice/sn0239.html.

[Kno79] Glenn F. Knoll. *Radiation Detection and Measurement.* John Wiley & Sons, New York, 2nd edition, 1979.

[L$^+$97] C. Lu et al. A detector scenario for the muon cooling experiment. Princeton/$\mu\mu$/**97-8**, http://puhep1.princeton.edu/~mcdonald/mumu/mumu-97-8.ps, July 1997.

[MN78] Jay N. Marx and David R. Nygren. The time projection chamber. *Phys. Today*, pages 46–53, October 1978.

[MO84] Ronald J. Madaras and Piermaria J. Oddone. Time-projection chambers. *Phys. Today*, pages 36–47, August 1984.

[Neu83] David Neuffer. Principles and applications of muon cooling. *Part. Acc.*, 14:75–90, 1983.

[Pal98] R.B. Palmer. Muon collider: Introduction and status. http://xxx.lanl.gov/ps/physics/9802005, February 1998.

[PEP76] Proposal for a PEP facility based on the time projection chamber, December 1976. PEP Proposal 4, Johns Hopkins University, Lawrence Berkeley Laboratory, University of California at Los Angeles, University of California at Riverside, Yale University.

[PG97] R.B. Palmer and J.C. Gallardo. High energy colliders. In M.A.E. Dementi V.L. Fitch, D.R. Marlow, editor, *Critical Problems in Physics*, pages 247–269, Princeton, 1997. Princeton University Press.

[PL69a] J.H. Parker and John J. Lowke. Theory of electron diffusion parallel to electic fields I: Theory. *Phys. Rev.*, 181(1):290–301, May 1969.

[PL69b] J.H. Parker and John J. Lowke. Theory of electron diffusion parallel to electic fields II: Application to real gases. *Phys.Rev.*, 181(1):302–311, May 1969.

[Pre98] Eric J. Prebys. Princeton warm-bore magnet. Princeton/$\mu\mu$/**98-9**, http://viper.princeton.edu/~prebys/mucollider/magnet.ps, March 1998.

[PS75] V. Palladino and B. Sadoulet. Application of classical theory of electrons in gases to drift proportional chambers. *Nucl. Instr. and Meth.*, 128:323–335, 1975.

[PS83] V.V. Parkhomchuk and A.N. Skrinsky. Ionization cooling: Physics and applications. In F.T. Cole and R. Donaldson, editors, *Proceedings of the 12th International Conference on High Energy Accelerators*, pages 485–487, 1983.

[Sch86] B. Schmidt. *Drift and Diffusion von Elektronen in Methan and Methan-Edelgas-Mischungen.* PhD thesis, Univ. Heidelberg, Mischungen, 1986. unpublished.

[SP81] A.N. Skrinsky and V.V. Parkhomchuk. Methods of cooling beams of charged particles. *Sov. J. Part. Nucl.*, 12(3):1981, May-June 1981.

[Va'92] J. Va'vra. Wire chamber gases. *Nucl. Instr. and Meth.*, A323:34–47, 1992.

[vE65] A. von Engel. *Ionized Gases.* Oxford University Press, Oxford, 2nd edition, 1965.

[Wil50] D.H. Wilkinson. *Ionization Chambers and Counters.* Cambridge University Press, Cambridge, 1950.